

# Monopulse Parameter Estimation based on MIMO-STCA Radar in the Presence of Multiple Mainlobe Jammings

Huake Wang\*, *Member, IEEE*, Dongchang Zhang, Guisheng Liao, *Senior Member, IEEE*, and Yinghui Quan, *Member, IEEE*

**Abstract**—The monopulse technique is characterized by its high accuracy in angle estimation and simplicity in engineering implementation. However, in the complex electromagnetic environment, the presence of the mainlobe jamming (MLJ) greatly degrades the accuracy of angle estimation. Conventional methods of jamming suppression often lead to significant deviations in monopulse ratio while suppressing MLJ. Additionally, the monopulse technique based on traditional radar cannot jointly estimate the target's range. In this paper, the four-channel adaptive beamforming (ABF) algorithm is proposed, which adds a delta-delta channel based on conventional sum-difference-difference three-channel to suppress a single MLJ. Moreover, considering the suppression of multiple MLJs and sidelobe jammings (SLJs), the row-column ABF algorithm is proposed. This algorithm utilizes more spatial degrees of freedom (DOFs) to suppress multiple jammings by the row-column adaptive beamforming at the subarray level. The key ideal of both algorithms is to suppress MLJ with null along one spatial direction while keeping the sum and difference beampatterns undistorted along another spatial direction. Therefore, the monopulse ratio remains undistorted while suppressing the MLJ, ensuring the accuracy of monopulse parameter estimation. Furthermore, by utilizing the additional degrees of freedom (DOFs) in the range domain provided by the multiple-input multiple-output space-time coding array (MIMO-STCA) radar, joint angle-range estimation can be achieved through the monopulse technique. Simulation results highlight the effectiveness of the proposed methods in suppressing multiple MLJs and enhancing the accuracy of monopulse parameter estimation, as verified by the low root mean square error (RMSE) in the parameter estimation results.

**Index Terms**—Monopulse technique; Adaptive beamforming; Multiple mainlobe jamming suppression; Parameter estimation.

## I. INTRODUCTION

THE Monopulse is a well-established technique for radar angle estimation [1], [2], [3], which is widely employed in modern radar systems [4]. The fundamental principle underlying the monopulse technique involves estimating the direction of the target by leveraging the ratio of the difference beam to the sum beam [5]. However, in the context of modern

battlefields, with the continuous upgrade of electronic defense systems, jamming techniques such as cross-eye jamming [6], angular glint jamming [7], and extremely high-power spot jamming [8] have significantly degraded the performance of the monopulse technique, especially when dealing with jamming signals that are in close proximity to the center of the mainlobe.

In order to suppress the mainlobe jamming (MLJ), several methods based on adaptive beamforming were proposed in [9], [10], [11]. However, due to the strong spatial correlation between the target and the MLJ, these methods often suppress the target signal alongside the MLJ, resulting in adverse effects such as mainlobe distortion, elevated sidelobe levels, and directional shifts. These issues lead to significant deviations in the monopulse ratio and a consequent reduction in parameter estimation accuracy [12]. In [13], [14], methods based on transmit polarization optimization have been proposed for suppressing MLJ. However, the effectiveness of these approaches may be significantly impacted by uncertainties in the electromagnetic environment. In [15], a mainlobe canceller employing adaptive digital beamforming was proposed for mainlobe jamming cancellation. However, this approach relies on precise alignment of the main beam with the target, which is challenging to accomplish in complex electromagnetic environments. A novel method for mainlobe jamming suppression leveraging the spatial polarization characteristics of antennas was proposed in [16]. However, this approach relies on accurate estimation of the polarization state of the MLJ, otherwise the effectiveness of MLJ suppression will be significantly compromised. In [17], [18], methods for MLJ suppression based on blind signal separation have been proposed, which can effectively separate the MLJ signal. However, these methods are associated with high computational complexity. For ground-based radar, a large auxiliary array was applied to suppress MLJ in [19]. However, the method requires a large place to configure the antenna, which is the limitation in practical applications. A MLJ suppression approach based on covariance matrix reconstruction was introduced in [20]. However, this method relies on prior knowledge of the MLJ's precise angle, which is challenging to obtain when limited training data is available. In [21], an adaptive monopulse approach with joint linear constraints on both the azimuth and elevation was proposed. This method flexibly adjusts the monopulse ratios for MLJ suppression at the subarray under constrained conditions, which is hard to determine.

This work was supported in part by the National Natural Science Foundation of China under Grants 62301410, in part by the Aviation Science Foundation under Grants 20230001081021, in part by the National Key Laboratory of Air-based Information Perception and Fusion under Grants ZH 2024-0053, and in part by the National Natural Science Foundation of China under Grants 62331019.

Huake Wang, Guisheng Liao and Yinghui Quan are with School of Electronic Engineering, Xidian University, Xi'an, Shaanxi, China, 710071. Huake Wang, Dongchang Zhang, Guisheng Liao and Yinghui Quan are with Hangzhou Institute of Technology, Xidian University, Hangzhou, Zhejiang, China, 311231.

As a widely known radar framework, the multiple-input multiple-output (MIMO) radar can transmit diverse mutually orthogonal waveforms simultaneously and employ multiple antennas to receive reflected signals, facilitating flexible spatial coverage [22], [23], [24]. Compared to a standard phased array, waveform diversity offers several advantages, including higher resolution [25], better parameter identifiability [26] and higher sensitivity to detecting slowly moving targets [27]. As a novel transmit diversity technique, space-time coding array (STCA) has aroused great research interest nowadays [28], [29], [30], [31]. The fundamental concepts and characteristics of STCA were first proposed in [32], along with introducing fundamental tools and evaluation criteria for assessing STCA radar performance. As an innovative radar system built upon colocated MIMO radar, STCA introduces the time shift among transmit elements. This characteristic enables the beam pattern of the STCA radar to be not only angle-dependent but also range-dependent. Regarding the application of STCA radar, [33] proposed a beamspace multiple signal classification (MUSIC) algorithm to address the problem of direction-of-arrival (DOA) estimation in the case of small training samples. In [34], a simplified method based on the space-time coding principle was proposed, which simplifies the beam pattern synthesis problem as a single waveform spectral shaping issue, enabling the generation of controllable transmit beam patterns with a lower computational complexity.

Notice that monopulse technique based on traditional radar cannot jointly estimate the target range. Combining existing MIMO technique [35], [36], [37], [38], [39], [40], [41] with STCA technique, the MIMO-STCA radar can extract DOFs in the range domain through signal processing at the receive end. In this paper, the extra DOFs provided by the MIMO-STCA radar in the range domain are exploited to achieve joint angle-range estimation. Notice the problem that the presence of MLJ degrades monopulse performance, and conventional suppression methods often cause adverse effects. Consequently, utilizing the characteristic that the beam pattern of a two-dimensional rectangular array is the product of independent row and column beam pattern, the four-channel ABF algorithm is proposed. This algorithm suppresses MLJ with null along one direction while keeping the sum-and-difference beam patterns undistorted along another direction. First, set the time shift equal to 0, the MIMO-STCA radar degrades to a conventional MIMO radar, and the planar array becomes an azimuth-elevation two-dimensional planar array. Thus, MLJ suppression is applied along azimuth direction while preserving sum-and-difference beam patterns in elevation direction, ensuring unbiased elevation estimation. Similarly, we can achieve unbiased azimuth angle estimation. Second, set the time shift to a non-zero value and apply elevation angle dependence compensation to the vertical steering vector, transforming the MIMO-STCA radar into an azimuth-range two-dimensional planar array. Accordingly, we can perform unbiased estimation of target range. Moreover, the row-column ABF algorithm is proposed to suppress multiple MLJs and sidelobe jammings (SLJs) simultaneously. Compared to the four-channel ABF algorithm, the row-column ABF algorithm reverses the order of ABF and monopulse beamforming.

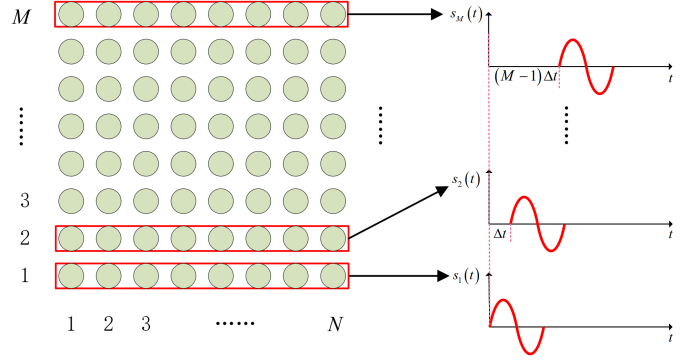


Fig. 1. MIMO-STCA planar array signal model

Specifically, each row or column is utilized as a subarray for ABF, thus more DOFs are exploited to suppress multiple jammings. Then, monopulse beamforming is performed along column or row to jointly estimate angle and range.

The innovations proposed in this paper are summarized as follows:

1) A new joint angle-range estimation method for MIMO-STCA radar is proposed. Utilizing the extra DOF in range domain introduced by STCA radar, sum-and-difference beams in range domain are formed after ABF. Then, the ratio of the difference beam to the sum beam is used for range estimation.

2) A new method for MLJ suppression in monopulse parameters estimation is proposed. The key idea is canceling MLJ with null along one direction while keeping the sum-and-difference beam patterns undistorted along another direction. This approach can suppress MLJ while maintaining undistorted monopulse ratio for unbiased parameters estimation.

3) A new method for suppressing multiple MLJs and SLJs at subarray level is proposed. First, analog beamforming is performed at element level and subarray outputs are converted to digital signals. Then, adaptive row and column digital beams are formed at subarray level, utilizing the multiple DOFs to adaptively suppress multiple jammings.

*Notations:* The remainder of this paper is organized as follows. Section II derives the signal model for MIMO-STCA radar. To enhance the accuracy of monopulse parameters estimation in the presence of MLJ, the four-channel ABF algorithm is introduced in Section III. Then, in Section IV, row-column ABF algorithm is proposed to suppress multiple jammings. The simulation results are given in Section V, and conclusions are finally drawn in Section VI.

## II. MIMO-STCA RADAR SIGNAL MODEL

In this paper, we propose the design of MIMO-STCA radar, which introduces the transmitted time shift among transmit elements in different rows. Consider the planar array of MIMO-STCA radar is composed of  $M$  rows and  $N$  columns of elements. All elements are uniformly distributed with half-wavelength spacing between adjacent elements. The signal model is shown in Fig. 1. The transmitted time delay for each element in the  $m$ th row can be represented as

$$\tau_m = (m - 1)\Delta t \quad (1)$$

where  $\Delta t$  is the time shift among transmit array elements in different rows.

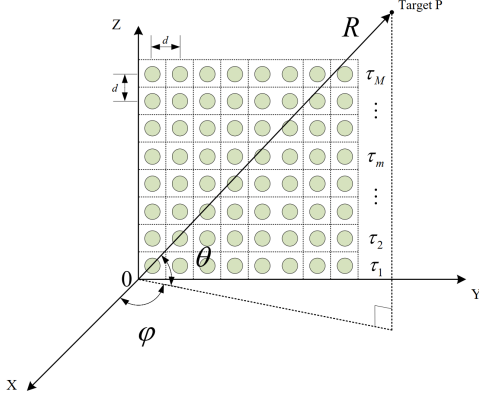


Fig. 2. The two-dimensional coordinate system for MIMO-STCA planar array

The MIMO-STCA radar antenna planar array is vertically placed on a horizontal plane, establishing the antenna planar array coordinate system as depicted in Fig. 2. In this figure,  $\varphi$  and  $\theta$  are azimuth angle and elevation angle, respectively.  $R$  is the range between target and the radar array.

Assume the transmitted signal is a narrow-band signal. The orthogonal signal  $\varphi_m(t)$  can be represented as:

$$\varphi_m(t) = c_m g(t) \quad (2)$$

where  $c_m$  is the orthogonal coded signal,  $g(t)$  is the linear frequency modulated (LFM) signal.

$$\int_T \varphi_m(t) \varphi_{m'}(t) dt = 0, \forall m, m' = 1, 2, \dots, M, m \neq m' \quad (3)$$

$$g(t) = \text{rect}\left(\frac{t}{T_p}\right) \exp(j\pi\mu t^2) \quad (4)$$

where  $T_p$  is the pulse duration,  $\mu = B/T_p$  and  $B$  is the bandwidth.

The signal transmitted by each element in the  $m$ th row can be represented as

$$S_m(t) = c_m g(t - \tau_m) \exp(j2\pi f_0 t) \quad (5)$$

where  $f_0$  is the carrier frequency.

Assume a far-field point target P located at azimuth angle  $\varphi$ , elevation angle  $\theta$ , and range  $R$  from the antenna array. Consider the origin element as the reference element, the unit vector in the direction of target P can be represented as  $(u, v)$ , where  $u = \cos\theta \sin\varphi$ ,  $v = \sin\theta$ . Therefore, the transmitted signal phase shift between the reference element and the element at the  $m$ th row and  $n$ th column is given by

$$\begin{aligned} \alpha_{(m,n)} &= \frac{2\pi}{\lambda} ((n-1)du + (m-1)dv) \\ &= (n-1)\alpha_y + (m-1)\alpha_z \end{aligned} \quad (6)$$

where  $\lambda = c/f_0$  is the wavelength,  $d$  represents the spacing between the adjacent elements. The superimposed transmitted signal from all MIMO-STCA radar elements can be given by

$$\begin{aligned} S(t) &= \sum_{n=1}^N \sum_{m=1}^M e^{j(m-1)\alpha_z} e^{j(n-1)\alpha_y} s_m(t) \\ &\approx e^{j2\pi f_0 t} \sum_{n=1}^N \sum_{m=1}^M \varphi_m(t) e^{j(n-1)\alpha_y} e^{j(m-1)\alpha_z} e^{-j2\pi\mu(m-1)t\Delta t} \mathbf{a}_z(\theta, R) \end{aligned} \quad (7)$$

Under the narrow-band assumption, the signal received by

target P can be expressed as

$$S\left(t - \frac{\tau}{2}\right) = e^{j2\pi f_0(t - \frac{\tau}{2})} \sum_{n=1}^N \sum_{m=1}^M \varphi_m\left(t - \frac{\tau}{2}\right) e^{j(n-1)\alpha_y} e^{j(m-1)\alpha_z} e^{-j2\pi\mu(m-1)(t - \frac{R}{c})\Delta t} \quad (8)$$

where  $\tau = 2R/c$  is the round-trip delay time between radar and target. Further, the radar echo received by the  $m'$ th ( $m' = 1, 2, \dots, M$ ) row and  $n'$ th ( $n' = 1, 2, \dots, N$ ) column element from target P's reflection can be represented as

$$x_{(m',n')}(t) = \xi_s e^{j(n'-1)\alpha_y} e^{j(m'-1)\alpha_z} S(t - \tau) \quad (9)$$

where  $\xi_s$  is the complex reflection coefficient of the target. The output of the received signal at the  $m$ th row and  $n$ th column element after down-conversion can be obtained as

$$\hat{x}_{(m',n')}(t) = x_{(n',m')}(t) \cdot e^{-j2\pi f_0 t} \quad (10)$$

Before matched filtering, it is necessary to digitally mix the received signal from each receive element with  $\Delta t$ , which can be represented as

$$\begin{aligned} \tilde{x}_{(m',n')}(t) &= \hat{x}_{(m',n')}(t) \bullet e^{j2\pi\mu(m'-1)t\Delta t} \\ &= \xi_s e^{-j2\pi f_0 \tau} \frac{1 - e^{jN\alpha_y}}{1 - e^{j\alpha_y}} e^{j(n'-1)\alpha_y} e^{j(m'-1)\alpha_z} \\ &\quad \varphi_{m'}(t - \tau) e^{j(m'-1)\alpha_z} e^{j2\pi\mu(m'-1)\Delta t} \\ &\quad + \xi_s e^{-j2\pi f_0 \tau} \frac{1 - e^{jN\alpha_y}}{1 - e^{j\alpha_y}} e^{j(n'-1)\alpha_y} e^{j(m'-1)\alpha_z} \\ &\quad \times \sum_{m=1, m \neq m'}^M \varphi_m(t - \tau) e^{j(m-1)\alpha_z} \\ &\quad e^{-j2\pi\mu(m-1)(t - \frac{2R}{c})\Delta t} e^{j2\pi\mu(m'-1)t\Delta t} \end{aligned} \quad (11)$$

Design matched filter functions for each receive element in the  $m'$ th row as  $h_{m'}(t) = \varphi_{m'}^*(-t)$ . Moreover, since  $\varphi_m(t)$  satisfies the orthogonality condition, the output of the matched filter can be obtained as

$$\begin{aligned} \bar{x}_{(m',n')}(t) &= \tilde{x}_{(m',n')}(t) * h_{m'}(t) \\ &= \beta_s e^{j(n'-1)\alpha_y} e^{j2(m'-1)\alpha_z} e^{j4\pi\mu\frac{R}{c}(m'-1)\Delta t} \end{aligned} \quad (12)$$

where  $*$  denotes the convolution operation,  $\beta_s = \xi_s e^{-j2\pi f_0 \tau} \frac{1 - e^{jN\alpha_y}}{1 - e^{j\alpha_y}}$  is the complex envelope of the received signal. Finally, the matched filter output for each element can be expressed as a vector, with the form as

$$\begin{aligned} \mathbf{X}_s &= [\bar{x}_{(1,1)}(t), \bar{x}_{(1,2)}(t), \dots, \bar{x}_{(1,N)}(t), \\ &\quad \bar{x}_{(2,1)}(t), \bar{x}_{(2,2)}(t), \dots, \bar{x}_{(M,N)}(t)]^T \\ &= \beta_s \mathbf{a}_z(\theta, R) \otimes \mathbf{a}_y(\theta, \varphi) = \beta_s \mathbf{v}(\theta, \varphi, R) \end{aligned} \quad (13)$$

where  $\otimes$  denotes the Kronecker product,  $\mathbf{v}(\theta, \varphi, R) \in \mathbb{C}^{MN \times 1}$ ,  $\mathbf{a}_y(\theta, \varphi) \in \mathbb{C}^{N \times 1}$  and  $\mathbf{a}_z(\theta, R) \in \mathbb{C}^{M \times 1}$  denote the array steering vector, the horizontal steering vector and vertical steering vector, respectively, which are expressed as

$$\begin{aligned} \mathbf{a}_y(\theta, \varphi) &= [1, e^{j\alpha_y}, \dots, e^{j(N-1)\alpha_y}]^T \\ &= [1, e^{j2\pi\frac{d}{\lambda} \cos\theta \sin\varphi}, \dots, e^{j2\pi\frac{d}{\lambda} (N-1) \cos\theta \sin\varphi}]^T \end{aligned} \quad (14)$$

$$\begin{aligned} \mathbf{a}_z(\theta, R) &= [1, e^{j2\alpha_z} e^{j4\pi\mu\frac{R}{c}\Delta t}, \dots, e^{j2(M-1)\alpha_z} e^{j4\pi\mu\frac{R}{c}(M-1)\Delta t}]^T \\ &= [1, e^{j4\pi(\frac{d}{\lambda} \sin\theta + \mu\frac{R}{c}\Delta t)}, \dots, e^{j4\pi(M-1)(\frac{d}{\lambda} \sin\theta + \mu\frac{R}{c}\Delta t)}]^T \end{aligned} \quad (15)$$

It can be observed that for MIMO-STCA radar, the horizontal steering vector is dependent solely on angle, while the vertical steering vector is a two-dimensional function of elevation angle and range. In contrast to traditional MIMO radar, it exhibits an extra degree of freedom in range domain. When the time shift in MIMO-STCA radar is set equal to 0, the vertical steering vector reduces to a function that depends only on the elevation angle. Therefore, its signal model is the same as that of the traditional MIMO radar.

Similarly, for a jammer with location  $(\varphi_j, \theta_j, R_j)$ , which can generate MLJ, the jamming signal can be expressed as

$$\mathbf{x}_j = \beta_j \mathbf{a}_z(\theta_j, R_j) \otimes \mathbf{a}_y(\theta_j, \varphi_j) = \beta_j \mathbf{v}(\theta_j, \varphi_j, R_j) \quad (16)$$

where  $\beta_j$  is the complex envelope of the jamming signal. Therefore, the received signal can be expressed as

$$\mathbf{x} = \mathbf{x}_s + \mathbf{x}_j + \mathbf{x}_n \quad (17)$$

where  $\mathbf{x}_n$  is the noise component, which can be assumed to be zero-mean white Gaussian distributed.

### III. FOUR-CHANNEL ADAPTIVE BEAMFORMING ALGORITHM FOR MLJ SUPPRESSION

In this section, we propose a four-channel adaptive beamforming algorithm, which introduces delta-delta beam as the auxiliary channel and utilizes sum-and-difference beamforming for adaptive MLJ cancellation. The key idea is suppressing MLJ with null along one direction while keeping the sum and difference beampatterns undistorted along another direction.

#### A. Azimuth-elevation two-dimensional signal processing

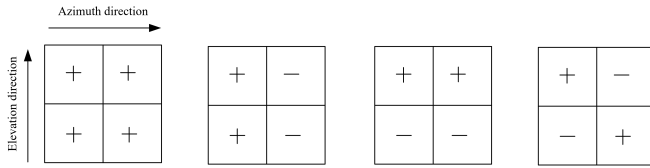


Fig. 3. Azimuth-elevation four-channel beamforming diagram. (a) Sum beam. (b) Delta-azimuth beam. (c) Delta-elevation beam. (d) Delta-delta beam

First, set  $\Delta t$  equal to 0, thus the vertical steering vector changes to  $\mathbf{a}_{ze}(\theta) = [1, e^{j4\pi \frac{d}{\lambda} \sin \theta}, \dots, e^{j4\pi(M-1)\frac{d}{\lambda} \sin \theta}]^T$ , which is only dependent on the elevation angle, thus the array steering vector changes to  $\mathbf{v}(\theta, \varphi) = \mathbf{a}_{ze}(\theta) \otimes \mathbf{a}_y(\theta, \varphi)$ . As a result, the planar array becomes an azimuth-elevation two-dimensional planar array. Second, as shown in Fig. 3, the two-dimensional planar array is divided into four parts: upper-left, lower-left, upper-right, and lower-right, with the digital beam output denoted as  $f_1, f_2, f_3$  and  $f_4$ , respectively. We can obtain the quiescent four-channel beams named two-dimensional sum beam  $f_\Sigma$ , delta-azimuth beam  $f_{\Delta_A}$ , delta-elevation beam  $f_{\Delta_E}$ , and delta-delta beam  $f_{\Delta\Delta}$  as

$$\begin{cases} f_\Sigma = (f_1 + f_2) + (f_3 + f_4) \\ f_{\Delta_A} = (f_1 + f_2) - (f_3 + f_4) \\ f_{\Delta_E} = (f_1 + f_3) - (f_2 + f_4) \\ f_{\Delta\Delta} = (f_1 + f_4) - (f_2 + f_3) \end{cases} \quad (18)$$

Suppose the MIMO-STCA radar beam is directed to  $(\varphi_0, \theta_0, R_0)$  and the target location is  $(\varphi_s, \theta_s, R_s)$ , the received signals of each element are weighted by  $\mathbf{W}_{\Sigma-\Sigma} = \mathbf{a}_{ze}(\theta_0) \otimes \mathbf{a}_y(\theta_0, \varphi_0)$ , thus we can obtain the two-dimensional quiescent sum beampattern as

$$\begin{aligned} g_\Sigma(u, v) &= \mathbf{W}_{\Sigma-\Sigma}^H \mathbf{v}(\theta, \varphi) \\ &= \sum_{m=1}^M \sum_{n=1}^N e^{j[(n-1)(\alpha_y - \alpha_{y0}) + 2(m-1)(\alpha_z - \alpha_{z0})]} \\ &= \sum_{n=1}^N e^{j(n-1)(\alpha_y - \alpha_{y0})} \times \sum_{m=1}^M e^{j2(m-1)(\alpha_z - \alpha_{z0})} \\ &= g_{\Sigma_a}(u) \times g_{\Sigma_e}(v) \end{aligned} \quad (19)$$

This indicates that the beampattern of a two-dimensional rectangular array is the product of independent row and column beampattern. This independence allows MLJ cancellation along one direction while keeping the sum and difference beampatterns undistorted along another direction.

Moreover, (18) can be rewritten as

$$\begin{cases} f_\Sigma = \beta_s g_\Sigma(u_s, v_s) + \beta_j g_\Sigma(u_j, v_j) + n_\Sigma \\ f_{\Delta_A} = \beta_s g_{\Delta_A}(u_s, v_s) + \beta_j g_{\Delta_A}(u_j, v_j) + n_{\Delta_A} \\ f_{\Delta_E} = \beta_s g_{\Delta_E}(u_s, v_s) + \beta_j g_{\Delta_E}(u_j, v_j) + n_{\Delta_E} \\ f_{\Delta\Delta} = \beta_s g_{\Delta\Delta}(u_s, v_s) + \beta_j g_{\Delta\Delta}(u_j, v_j) + n_{\Delta\Delta} \end{cases} \quad (20)$$

where  $n$  is the white Gaussian noise. As shown in (21), using the sum beam as the main beam and the delta-elevation beam as the auxiliary beam for adaptive jamming cancellation, we obtain the adaptive azimuth-sum beam output  $\hat{f}_{\Sigma_A}$ . Similarly, we can obtain the adaptive azimuth-difference beam output  $\hat{f}_{\Delta_A}$ , the adaptive elevation-sum beam output  $\hat{f}_{\Sigma_E}$  and the adaptive elevation-difference beam output  $\hat{f}_{\Delta_E}$ .

$$\begin{cases} \hat{f}_{\Sigma_A} = f_\Sigma - w_{a1} f_{\Delta_E} \\ \hat{f}_{\Delta_A} = f_{\Delta_A} - w_{a2} f_{\Delta\Delta} \end{cases} \quad (21a)$$

$$\begin{cases} \hat{f}_{\Sigma_E} = f_\Sigma - w_{e1} f_{\Delta_A} \\ \hat{f}_{\Delta_E} = f_{\Delta_E} - w_{e2} f_{\Delta\Delta} \end{cases} \quad (21b)$$

where  $w_{a1}, w_{a2}, w_{e1}$  and  $w_{e2}$  denote the adaptive weights, which are estimated from the sample values of the quiescent four-channel beams as

$$w_{a1} = \frac{E[f_\Sigma f_{\Delta_E}^*]}{E[f_{\Delta_E} f_{\Delta_E}^*]}, w_{a2} = \frac{E[f_{\Delta_A} f_{\Delta\Delta}^*]}{E[f_{\Delta\Delta} f_{\Delta\Delta}^*]} \quad (22a)$$

$$w_{e1} = \frac{E[f_\Sigma f_{\Delta_A}^*]}{E[f_{\Delta_A} f_{\Delta_A}^*]}, w_{e2} = \frac{E[f_{\Delta_E} f_{\Delta\Delta}^*]}{E[f_{\Delta\Delta} f_{\Delta\Delta}^*]} \quad (22b)$$

According to the correlation theory, we can obtain

$$E[f_\Sigma f_{\Delta_E}^*] = P_j g_\Sigma(u_j, v_j) g_{\Delta_E}^*(u_j, v_j) + P_s g_\Sigma(u_s, v_s) g_{\Delta_E}^*(u_s, v_s) \quad (23a)$$

$$E[f_{\Delta_E} f_{\Delta_E}^*] = P_j g_{\Delta_E}(u_j, v_j) g_{\Delta_E}^*(u_j, v_j) + P_s g_{\Delta_E}(u_s, v_s) g_{\Delta_E}^*(u_s, v_s) + P_n \quad (23b)$$

$$E[f_{\Delta_A} f_{\Delta\Delta}^*] = P_j g_{\Delta_A}(u_j, v_j) g_{\Delta\Delta}^*(u_j, v_j) + P_s g_{\Delta_A}(u_s, v_s) g_{\Delta\Delta}^*(u_s, v_s) \quad (23c)$$

$$E[f_{\Delta\Delta} f_{\Delta\Delta}^*] = P_j g_{\Delta\Delta}(u_j, v_j) g_{\Delta\Delta}^*(u_j, v_j) + P_s g_{\Delta\Delta}(u_s, v_s) g_{\Delta\Delta}^*(u_s, v_s) + P_n \quad (23d)$$

$$E[f_\Sigma f_{\Delta_A}^*] = P_j g_\Sigma(u_j, v_j) g_{\Delta_A}^*(u_j, v_j) + P_s g_\Sigma(u_s, v_s) g_{\Delta_A}^*(u_s, v_s) \quad (23e)$$

$$E[f_{\Delta_A} f_{\Delta_A}^*] = P_j g_{\Delta_A}(u_j, v_j) g_{\Delta_A}^*(u_j, v_j) + P_s g_{\Delta_A}(u_s, v_s) g_{\Delta_A}^*(u_s, v_s) + P_n \quad (23f)$$

$$E[f_{\Delta_E} f_{\Delta\Delta}^*] = P_j g_{\Delta_E}(u_j, v_j) g_{\Delta\Delta}^*(u_j, v_j) + P_s g_{\Delta_E}(u_s, v_s) g_{\Delta\Delta}^*(u_s, v_s) \quad (23g)$$



where  $P_s, P_j$  and  $P_n$  are the power of the target echo, MLJ and noise, respectively. Because  $P_j \gg P_s, P_j \gg P_n$ , we obtain

$$\begin{cases} w_{a1} = \frac{E[f_{\Sigma} f_{\Delta_E}^*]}{E[f_{\Delta_E} f_{\Delta_E}^*]} \approx \frac{g_{\Sigma}(u_j, v_j)}{g_{\Delta_E}(u_j, v_j)} = \frac{g_{\Sigma_e}(v_j)}{g_{\Delta_e}(v_j)} \\ w_{a2} = \frac{E[f_{\Delta_A} f_{\Delta_E}^*]}{E[f_{\Delta_A} f_{\Delta_A}^*]} \approx \frac{g_{\Delta_A}(u_j, v_j)}{g_{\Delta_A}(u_j, v_j)} = \frac{g_{\Sigma_e}(v_j)}{g_{\Delta_e}(v_j)} \end{cases} \quad (24a)$$

$$\begin{cases} w_{e1} = \frac{E[f_{\Sigma} f_{\Delta_A}^*]}{E[f_{\Delta_A} f_{\Delta_A}^*]} \approx \frac{g_{\Sigma}(u_j, v_j)}{g_{\Delta_A}(u_j, v_j)} = \frac{g_{\Sigma_a}(u_j)}{g_{\Delta_a}(u_j)} \\ w_{e2} = \frac{E[f_{\Delta_E} f_{\Delta_A}^*]}{E[f_{\Delta_E} f_{\Delta_E}^*]} \approx \frac{g_{\Delta_E}(u_j, v_j)}{g_{\Delta_E}(u_j, v_j)} = \frac{g_{\Sigma_a}(u_j)}{g_{\Delta_a}(u_j)} \end{cases} \quad (24b)$$

It is obvious that  $w_{a1} = w_{a2} = w_a, w_{e1} = w_{e2} = w_e$ . Thus, the adaptive four-channel beams can be rewritten as

$$\begin{cases} \hat{f}_{\Sigma_A} = \beta_s (g_{\Sigma}(u_s, v_s) - w_a g_{\Delta_E}(u_s, v_s)) + n_{\Sigma} - w_a n_{\Delta_E} \\ \hat{f}_{\Delta_A} = \beta_s (g_{\Delta_A}(u_s, v_s) - w_a g_{\Delta_A}(u_s, v_s)) + n_{\Delta_A} - w_a n_{\Delta_A} \end{cases} \quad (25a)$$

$$\begin{cases} \hat{f}_{\Sigma_E} = \beta_s (g_{\Sigma}(u_s, v_s) - w_e g_{\Delta_A}(u_s, v_s)) + n_{\Sigma} - w_e n_{\Delta_A} \\ \hat{f}_{\Delta_E} = \beta_s (g_{\Delta_E}(u_s, v_s) - w_e g_{\Delta_A}(u_s, v_s)) + n_{\Delta_E} - w_e n_{\Delta_A} \end{cases} \quad (25b)$$

where the jamming is suppressed, and we can obtain the adaptive monopulse ratios in azimuth dimension and elevation dimension as

$$\hat{m}_a = \frac{\hat{f}_{\Delta_A}}{\hat{f}_{\Sigma_A}} \approx \frac{g_{\Delta_A}(u_s, v_s) - w_a g_{\Delta_A}(u_s, v_s)}{g_{\Sigma}(u_s, v_s) - w_a g_{\Delta_E}(u_s, v_s)} = \frac{g_{\Delta_a}(u_s)}{g_{\Sigma_a}(u_s)} = m_a \quad (26a)$$

$$\hat{m}_e = \frac{\hat{f}_{\Delta_E}}{\hat{f}_{\Sigma_E}} \approx \frac{g_{\Delta_E}(u_s, v_s) - w_e g_{\Delta_A}(u_s, v_s)}{g_{\Sigma}(u_s, v_s) - w_e g_{\Delta_A}(u_s, v_s)} = \frac{g_{\Delta_e}(v_s)}{g_{\Sigma_e}(v_s)} = m_e \quad (26b)$$

where  $m_a$  and  $m_e$  are the quiescent monopulse ratios in azimuth dimension and elevation dimension, respectively. (26) shows that the adaptive monopulse ratio along the azimuth (elevation) direction is maintained while canceling the MLJ along the elevation (azimuth) direction. In conclusion, the adaptive output ratio can still be utilized for angle estimation.

### B. Azimuth-range two-dimensional signal processing

After the above process, setting  $\Delta t = 1/B$ , and we have determined the elevation angle  $\theta$ , so we can apply elevation angle dependence compensation to the vertical steering vector  $\mathbf{a}_z(\theta, R)$ , which can be represented as

$$\begin{aligned} \mathbf{a}_{zr}(R) &= \mathbf{a}_z(\theta, R) \odot \mathbf{c}(\theta) \\ &= [1, e^{j4\pi\mu\frac{R}{c}\Delta t}, \dots, e^{j4\pi(M-1)\mu\frac{R}{c}\Delta t}]^T \end{aligned} \quad (27)$$

where  $\mathbf{c}(\theta) = [1, e^{-j2\pi\frac{d}{\lambda}\sin\theta}, \dots, e^{-j2\pi\frac{d}{\lambda}(M-1)\sin\theta}]^T$ ,  $\odot$  denotes the Hadamard product. After compensation, the vertical steering changes to  $\mathbf{a}_{zr}(R)$ , which is solely dependent on the range. Thus, the planar array becomes an azimuth-range two-dimensional planar array.

Similar to azimuth-elevation two-dimensional planar array, we can obtain the output from upper-left part, lower-left part, upper-right part and lower-right part, denoting them as  $r_1, r_2, r_3$  and  $r_4$ , respectively. And we can also obtain the quiescent four-channel beams as

$$\begin{cases} r_{\Sigma} = (r_1 + r_2) + (r_3 + r_4) \\ r_{\Delta_A} = (r_1 + r_2) - (r_3 + r_4) \\ r_{\Delta_R} = (r_1 + r_3) - (r_2 + r_4) \\ r_{\Delta_{\Delta}} = (r_1 + r_4) - (r_2 + r_3) \end{cases} \quad (28)$$

The received signals of each element are weighted by  $\mathbf{W}'_{\Sigma-\Sigma} = \mathbf{a}_{zr}(R_0) \otimes \mathbf{a}_y(\theta_0, \varphi_0)$ , thus the azimuth-range two-dimensional quiescent sum beampattern is

$$\begin{aligned} p_{\Sigma}(u, R) &= \mathbf{W}'_{\Sigma-\Sigma}^H [\mathbf{a}_{zr}(R) \otimes \mathbf{a}_y(\theta, \varphi)] \\ &= \sum_{m=1}^M \sum_{n=1}^N e^{j((n-1)(\alpha_y - \alpha_{y0}) + 4(m-1)\pi\mu\frac{(R-R_0)}{c}\Delta t)} \\ &= \sum_{n=1}^N e^{j((n-1)(\alpha_y - \alpha_{y0}))} \times \sum_{m=1}^M e^{j4(m-1)\pi\mu\frac{(R-R_0)}{c}\Delta t} \\ &= p_{\Sigma_a}(u) \times p_{\Sigma_r}(R) \end{aligned} \quad (29)$$

Then, we can rewrite the four-channel beams as

$$\begin{cases} r_{\Sigma} = \beta_s p_{\Sigma}(u_s, R_s) + \beta_j p_{\Sigma}(u_j, R_j) + n_{\Sigma} \\ r_{\Delta_A} = \beta_s p_{\Delta_A}(u_s, R_s) + \beta_j p_{\Delta_A}(u_j, R_j) + n_{\Delta_A} \\ r_{\Delta_R} = \beta_s p_{\Delta_R}(u_s, R_s) + \beta_j p_{\Delta_R}(u_j, R_j) + n_{\Delta_R} \\ r_{\Delta_{\Delta}} = \beta_s p_{\Delta_{\Delta}}(u_s, R_s) + \beta_j p_{\Delta_{\Delta}}(u_j, R_j) + n_{\Delta_{\Delta}} \end{cases} \quad (30)$$

Similar to azimuth-elevation two-dimensional planar array, the adaptive range sum and difference beams can be obtained as

$$\begin{cases} \hat{r}_{\Sigma_R} = r_{\Sigma} - w_{r1} r_{\Delta_A} \\ \hat{r}_{\Delta_R} = r_{\Delta_R} - w_{r2} r_{\Delta_{\Delta}} \end{cases} \quad (31)$$

where  $w_{r1}$  and  $w_{r2}$  denote the adaptive weights, which can be obtained as

$$w_{r1} = \frac{E[r_{\Sigma} r_{\Delta_A}^*]}{E[r_{\Delta_A} r_{\Delta_A}^*]}, w_{r2} = \frac{E[r_{\Delta_R} r_{\Delta_{\Delta}}^*]}{E[r_{\Delta_{\Delta}} r_{\Delta_{\Delta}}^*]} \quad (32)$$

According to the correlation theory, we can obtain

$$E[r_{\Sigma} r_{\Delta_A}^*] = P_s p_{\Sigma}(u_s, R_s) p_{\Delta_A}^*(u_s, R_s) + P_j p_{\Sigma}(u_j, R_j) p_{\Delta_A}^*(u_j, R_j) \quad (33a)$$

$$E[r_{\Delta_A} r_{\Delta_A}^*] = P_s p_{\Delta_A}(u_s, R_s) p_{\Delta_A}^*(u_s, R_s) + P_j p_{\Delta_A}(u_j, R_j) p_{\Delta_A}^*(u_j, R_j) + P_n \quad (33b)$$

$$E[r_{\Delta_R} r_{\Delta_{\Delta}}^*] = P_s p_{\Delta_R}(u_s, R_s) p_{\Delta_{\Delta}}^*(u_s, R_s) + P_j p_{\Delta_R}(u_j, R_j) p_{\Delta_{\Delta}}^*(u_j, R_j) \quad (33c)$$

$$E[r_{\Delta_{\Delta}} r_{\Delta_{\Delta}}^*] = P_s p_{\Delta_{\Delta}}(u_s, R_s) p_{\Delta_{\Delta}}^*(u_s, R_s) + P_j p_{\Delta_{\Delta}}(u_j, R_j) p_{\Delta_{\Delta}}^*(u_j, R_j) + P_n \quad (33d)$$

Similarly, since  $P_j \gg P_s, P_j \gg P_n$ , we can obtain

$$\begin{cases} w_{r1} = \frac{E[r_{\Sigma} r_{\Delta_A}^*]}{E[r_{\Delta_A} r_{\Delta_A}^*]} \approx \frac{p_{\Sigma}(u_j, R_j)}{p_{\Delta_A}(u_j, R_j)} = \frac{p_{\Sigma_a}(u_j)}{p_{\Delta_a}(u_j)} \\ w_{r2} = \frac{E[r_{\Delta_R} r_{\Delta_{\Delta}}^*]}{E[r_{\Delta_{\Delta}} r_{\Delta_{\Delta}}^*]} \approx \frac{p_{\Delta_R}(u_j, R_j)}{p_{\Delta_{\Delta}}(u_j, R_j)} = \frac{p_{\Sigma_a}(u_j)}{p_{\Delta_a}(u_j)} \end{cases} \quad (34)$$

It can be concluded that  $w_{r1} = w_{r2} = w_r$ , so we can obtain the adaptive range sum and difference beams as

$$\begin{cases} \hat{r}_{\Sigma_R} = \beta_s (p_{\Sigma}(u_s, R_s) - w_r p_{\Delta_A}(u_s, R_s)) + n_{\Sigma} - w_r n_{\Delta_A} \\ \hat{r}_{\Delta_R} = \beta_s (p_{\Delta_R}(u_s, R_s) - w_r p_{\Delta_{\Delta}}(u_s, R_s)) + n_{\Delta_R} - w_r n_{\Delta_{\Delta}} \end{cases} \quad (35)$$

Further, the ratio of the adaptive range difference beam to the sum beam is

$$\hat{m}_R = \frac{\hat{r}_{\Delta_R}}{\hat{r}_{\Sigma_R}} \approx \frac{p_{\Delta_R}(u_s, R_s) - w_r p_{\Delta_{\Delta}}(u_s, R_s)}{p_{\Sigma}(u_s, R_s) - w_r p_{\Delta_A}(u_s, R_s)} = \frac{p_{\Delta_r}(R_s)}{p_{\Sigma_r}(R_s)} = m_R \quad (36)$$

where  $m_R$  is the quiescent monopulse ratio in the range dimension. This equation indicates that the extra DOF in range dimension, which is introduced by MIMO-STCA radar can be used to estimate the target range. Furthermore, by maintaining the adaptive monopulse ratio in range dimension, ensuring the high performance of range estimation.

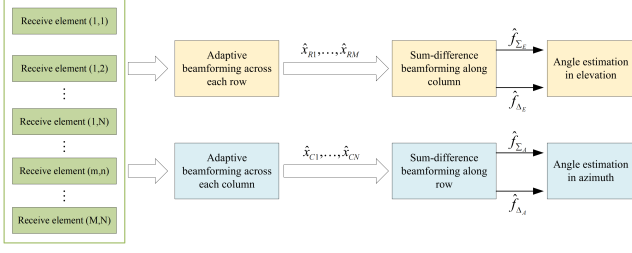


Fig. 4. Process of row-column adaptive beamforming algorithm

#### IV. ROW-COLUMN ADAPTIVE BEAMFORMING ALGORITHM FOR JOINT SUPPRESSION OF MULTIPLE MLJS AND SLJS

The four-channel adaptive beamforming algorithm uses 2 DOFs in both horizontal and vertical directions, limiting it to suppressing only one MLJ. To address this issue, we further propose the row-column adaptive beamforming algorithm for MIMO-STCA radar, enabling target angle and range joint estimation while suppressing multiple MLJs and SLJs. This algorithm first conducts adaptive jammings cancellation for each row or column. By treating each row or column as an adaptive subarray, multiple DOFs can be utilized to suppress multiple jammings simultaneously. Then, two-dimensional sum and difference beams can be obtained for parameters estimation.

##### A. Azimuth-elevation two-dimensional signal processing

With multiple MLJs and SLJs, assuming the number of jammings is  $N_J$ , the target location is  $(\theta_s, \varphi_s, R_s)$ , the received signal from the MIMO-STCA array elements is formed as

$$\mathbf{x} = \mathbf{x}_s + \sum_{n_j=1}^{N_J} \mathbf{x}_{n_j} + \mathbf{x}_n \quad (37)$$

Fig. 4 illustrates the row-column adaptive beamforming algorithm process. First, setting  $\Delta t = 0$  transforms the planar array into an azimuth-elevation two-dimensional planar array, similar to the four-channel adaptive beamforming algorithm. Second, 1-D adaptive beamforming is performed across each row or column to cancel multiple jammings. Third, adaptive sum and difference beams are formed in the other dimension independently. Finally, monopulse angle estimation is applied.

The jammings cancellation via adaptive beamforming is accomplished across rows and columns separately, illustrating in Fig. 5. The received data vectors for the  $m$ th row and the  $n$ th column are given as follows

$$\mathbf{x}_{Rm} = [x_{m,1}, x_{m,2}, \dots, x_{m,N}]^T, m = 1, 2, \dots, M \quad (38a)$$

$$\mathbf{x}_{Cn} = [x_{1,n}, x_{2,n}, \dots, x_{M,n}]^T, n = 1, 2, \dots, N \quad (38b)$$

The adaptive beamforming in the  $m$ th row is given as follows

$$\hat{x}_{Rm} = x_{m,1} + \hat{w}_{m,2}^R x_{m,2} + \dots + \hat{w}_{m,N}^R x_{m,N} \quad (39)$$

where  $w^R$  is the adaptive weight. The adaptive weight vector of the  $m$ th row can be written as

$$\hat{\mathbf{W}}_m^R = [1, \hat{w}_{m,2}^R, \dots, \hat{w}_{m,N}^R]^T \quad (40)$$

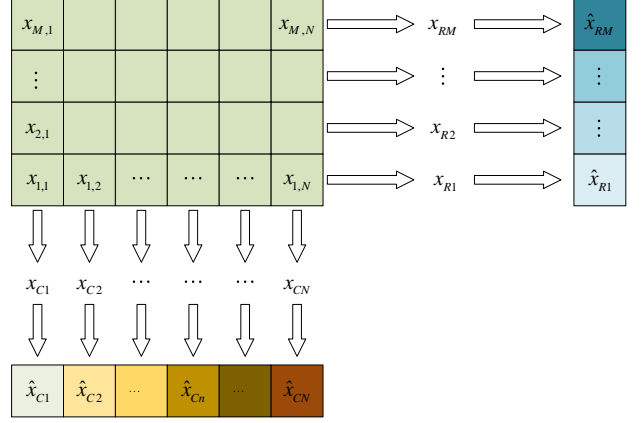


Fig. 5. Adaptive beamforming across rows and columns

The weight is computed using the minimum variance distortionless response (MVDR) method, expressing as follows

$$\begin{cases} \min (\hat{\mathbf{W}}_m^R)^H \mathbf{R}_{X_{Rm}} \hat{\mathbf{W}}_m^R \\ \text{s.t. } (\hat{\mathbf{W}}_m^R)^H \mathbf{a}_y(\theta_0, \varphi_0) = 1 \end{cases} \quad (41)$$

where  $\mathbf{R}_{X_{Rm}} = E[\mathbf{x}_{Rm} \mathbf{x}_{Rm}^H]$  is the sample covariance matrix of the received data vector in the  $m$ th row. The solution is derived using the Lagrange multiplier method, yielding the adaptive weight vector as

$$\begin{cases} \hat{\mathbf{W}}_m^R = \alpha (\mathbf{R}_{X_{Rm}})^{-1} \mathbf{a}_y(\theta_0, \varphi_0) \\ \alpha = 1 / (\mathbf{a}_y(\theta_0, \varphi_0))^H (\mathbf{R}_{X_{Rm}})^{-1} \mathbf{a}_y(\theta_0, \varphi_0) \end{cases} \quad (42)$$

The relationship between the steering vector of the  $m$ th row and the  $(m+1)$ th row can be represented as

$$\mathbf{v}_{m+1}(\theta, \varphi) = e^{j4\pi \frac{d}{\lambda} \sin \theta} \times \mathbf{v}_m(\theta, \varphi) \quad (43)$$

Consequently, the relationship between the adaptive weight vector of the  $m$ th row and the  $(m+1)$ th row can be represented as

$$\hat{\mathbf{W}}_{m+1}^R = e^{j4\pi \frac{d}{\lambda} \sin \theta} \times \hat{\mathbf{W}}_m^R \quad (44)$$

The output of adaptive beam in the  $m$ th row is given as

$$\hat{x}_{Rm} = (\hat{\mathbf{W}}_m^R)^H \mathbf{x}_{Rm} \quad (45)$$

The adaptive  $n$ th column beamforming in elevation dimension can be performed in a similar manner. The adaptive  $n$ th column beamforming is given by the following

$$\hat{x}_{Cn} = x_{1,n} + \hat{w}_{2,n}^C x_{2,n} + \dots + \hat{w}_{M,n}^C x_{M,n} \quad (46)$$

The adaptive weight vector of the  $n$ th column is given by

$$\hat{\mathbf{W}}_n^C = [1, \hat{w}_{2,n}^C, \dots, \hat{w}_{M,n}^C]^T \quad (47)$$

Similarly,  $\mathbf{W}_n^C$  can be obtained as follows

$$\begin{cases} \hat{\mathbf{W}}_n^C = \beta (\mathbf{R}_{X_{Cn}})^{-1} \mathbf{a}_{ze}(\theta_0) \\ \beta = 1 / (\mathbf{a}_{ze}(\theta_0))^H (\mathbf{R}_{X_{Cn}})^{-1} \mathbf{a}_{ze}(\theta_0) \end{cases} \quad (48)$$

where  $\mathbf{R}_{X_{Cn}}$  is the sample covariance matrix of the received data vector in the  $n$ th column. The relationship between the adaptive weight vector of the  $n$ th column and the  $(n+1)$ th

column can be represented as

$$\hat{\mathbf{W}}_{n+1}^C = e^{j2\pi \frac{d}{\lambda} \cos \theta \sin \varphi} \hat{\mathbf{W}}_n^C \quad (49)$$

The output of adaptive beam in the  $n$ th column is given

$$\hat{x}_{Cn} = (\hat{\mathbf{W}}_n^C)^H \mathbf{x}_{Cn} \quad (50)$$

### B. Azimuth-range two-dimensional signal processing

Similarly, the elevation angle dependence compensation is applied to the vertical steering vector  $\mathbf{a}_z(\theta, R)$ , transforming the planar array into an azimuth-range two-dimensional planar array. The jammings cancellation is accomplished in azimuth dimension. The received data vectors for the  $m$ th row are given as

$$\mathbf{y}_{Rm} = [y_{m,1}, y_{m,2}, \dots, y_{m,N}]^T, m = 1, 2, \dots, M \quad (51)$$

The adaptive beamforming in the  $m$ th row is given as

$$\hat{y}_{Rm} = y_{m,1} + w'_{m,2} y_{m,2} + \dots + w'_{m,N} y_{m,N} \quad (52)$$

The adaptive weight vector  $\mathbf{W}_m'^R$  can be written as

$$\mathbf{W}_m'^R = [1, w'_{m,2}, \dots, w'_{m,N}]^T \quad (53)$$

Similarly,  $\mathbf{W}_m'^R$  can be derived as follows

$$\begin{cases} \min (\mathbf{W}_m'^R)^H \mathbf{R}_{y_{Rm}} \mathbf{W}_m'^R \\ \text{s.t. } (\mathbf{W}_m'^R)^H \mathbf{a}_y(\theta_0, \varphi_0) = 1 \end{cases} \quad (54)$$

where  $\mathbf{R}_{y_{Rm}}$  is the sample covariance matrix of the received data vector in the  $m$ th row. Then, we can obtain

$$\begin{cases} \mathbf{W}_m'^R = \alpha (\mathbf{R}_{y_{Rm}})^{-1} \mathbf{a}_y(\theta_0, \varphi_0) \\ \alpha = 1 / (\mathbf{a}_y(\theta_0, \varphi_0))^H (\mathbf{R}_{y_{Rm}})^{-1} \mathbf{a}_y(\theta_0, \varphi_0) \end{cases} \quad (55)$$

The output of adaptive beam in the  $m$ th row is given by

$$\hat{y}_{Rm} = (\mathbf{W}_m'^R)^H \mathbf{y}_{Rm} \quad (56)$$

To sum up, all the  $M$  or  $N$  DOFs have been exploited in the adaptive row or column beamforming, which means theoretically up to  $M - 1$  or  $N - 1$  MLJs and/or SLJs can be adaptive suppressed across each row or each column.

### C. Adaptive monopulse parameters estimation

After the adaptive processing, the three adaptive beams in three dimensions are given as follows

$$\hat{\mathbf{x}}_E = [\hat{x}_{R1}, \hat{x}_{R2}, \dots, \hat{x}_{RM}] \quad (57a)$$

$$\hat{\mathbf{x}}_A = [\hat{x}_{C1}, \hat{x}_{C2}, \dots, \hat{x}_{CN}] \quad (57b)$$

$$\hat{\mathbf{x}}_R = [\hat{y}_{R1}, \hat{y}_{R2}, \dots, \hat{y}_{RM}] \quad (57c)$$

where  $\hat{x}_E, \hat{x}_A$  and  $\hat{x}_R$  represent the adaptive beams in elevation, azimuth and range dimensions, respectively. With adaptive column beam outputs, the sum-and-difference beams are formed along the row. Similarly, with adaptive row beam outputs, the sum-and-difference beams are formed along the column. Thus, the six monopulse beams are given as

$$\hat{f}_{\Sigma_E} = (\mathbf{w}_{\Sigma_E})^H \hat{\mathbf{x}}_E \quad \hat{f}_{\Delta_E} = (\mathbf{w}_{\Delta_E})^H \hat{\mathbf{x}}_E \quad (58a)$$

$$\hat{f}_{\Sigma_A} = (\mathbf{w}_{\Sigma_A})^H \hat{\mathbf{x}}_A \quad \hat{f}_{\Delta_A} = (\mathbf{w}_{\Delta_A})^H \hat{\mathbf{x}}_A \quad (58b)$$

$$\hat{f}_{\Sigma_R} = (\mathbf{w}_{\Sigma_R})^H \hat{\mathbf{x}}_R \quad \hat{f}_{\Delta_R} = (\mathbf{w}_{\Delta_R})^H \hat{\mathbf{x}}_R \quad (58c)$$

where  $\mathbf{w}_{\Sigma_E}, \mathbf{w}_{\Delta_E}, \mathbf{w}_{\Sigma_A}, \mathbf{w}_{\Delta_A}, \mathbf{w}_{\Sigma_R}$  and  $\mathbf{w}_{\Delta_R}$  are the quiescent sum and difference weight vectors along elevation, azimuth, and range dimensions, respectively, as if monopulse beamforming is performed on a ULA. They are given by

$$\mathbf{w}_{\Sigma_E} = \mathbf{a}_{ze}(\theta_0) \left[ 1, e^{j4\pi \frac{d}{\lambda} \sin \theta_0}, \dots, e^{j4\pi(M-1) \frac{d}{\lambda} \sin \theta_0} \right]^T \quad (59a)$$

$$\mathbf{w}_{\Delta_E} = \mathbf{a}_{ze}(\theta_0) \odot \mathbf{c}_{\Delta M} = \left[ 1, e^{j4\pi \frac{d}{\lambda} \sin \theta_0}, \dots, -e^{j4\pi(M-1) \frac{d}{\lambda} \sin \theta_0} \right]^T \quad (59b)$$

$$\mathbf{w}_{\Sigma_A} = \mathbf{a}_y(\theta_0, \varphi_0) = \left[ 1, e^{j2\pi \frac{d}{\lambda} \cos \theta_0 \sin \varphi_0}, \dots, e^{j2\pi \frac{d}{\lambda} (N-1) \cos \theta_0 \sin \varphi_0} \right]^T \quad (59c)$$

$$\begin{aligned} \mathbf{w}_{\Delta_A} &= \mathbf{a}_y(\theta_0, \varphi_0) \odot \mathbf{c}_{\Delta N} \\ &= \left[ 1, e^{j2\pi \frac{d}{\lambda} \cos \theta_0 \sin \varphi_0}, \dots, -e^{j2\pi \frac{d}{\lambda} (N-1) \cos \theta_0 \sin \varphi_0} \right]^T \end{aligned} \quad (59d)$$

$$\mathbf{w}_{\Sigma_R} = \mathbf{a}_{zr}(R_0) = \left[ 1, e^{j4\pi \mu \frac{R_0}{c} \Delta t}, \dots, e^{j4\pi(M-1) \mu \frac{R_0}{c} \Delta t} \right]^T \quad (59e)$$

$$\mathbf{w}_{\Delta_R} = \mathbf{a}_{zr}(R_0) \odot \mathbf{c}_{\Delta M} = \left[ 1, e^{j4\pi \mu \frac{R_0}{c} \Delta t}, \dots, -e^{j4\pi(M-1) \mu \frac{R_0}{c} \Delta t} \right]^T \quad (59f)$$

where  $\mathbf{c}_{\Delta} = [1, 1, \dots, -1, -1]$  is the difference vector, with the first half of elements as 1 and the second half as -1. Note that the six adaptive monopulse beams all have nulls at jamming angles and ranges, which means both MLJs and SLJs are successfully suppressed, thus they can be exploited for parameters estimation.

For elevation angle estimation, the adaptive elevation monopulse ratio is given by

$$\hat{m}_E = \frac{\hat{f}_{\Delta_E}}{\hat{f}_{\Sigma_E}} = \frac{(\mathbf{w}_{\Delta_E})^H \hat{\mathbf{x}}_E}{(\mathbf{w}_{\Sigma_E})^H \hat{\mathbf{x}}_E} = \frac{\hat{g}_{\Delta_E}(\theta_s, \varphi_s)}{\hat{g}_{\Sigma_E}(\theta_s, \varphi_s)} \quad (60)$$

Since the beampattern of a rectangular array is the product of independent row and column beampatterns, the adaptive monopulse beams in elevation dimension can be expressed as

$$\hat{g}_{\Sigma_E}(\theta_s, \varphi_s) = g_{\Sigma_e}(\theta_s) \times \hat{g}_{\Sigma_a}(\varphi_s) \quad (61a)$$

$$\hat{g}_{\Delta_E}(\theta_s, \varphi_s) = g_{\Delta_e}(\theta_s) \times \hat{g}_{\Delta_a}(\varphi_s) \quad (61b)$$

The beampatterns are separated into two parts,  $g$  denotes quiescent beampattern, and  $\hat{g}$  denotes adaptive beampattern. Substituting (61) into (60), the adaptive elevation monopulse ratio can be further given by

$$\hat{m}_E = \frac{\hat{g}_{\Delta_E}(\theta_s, \varphi_s)}{\hat{g}_{\Sigma_E}(\theta_s, \varphi_s)} = \frac{g_{\Delta_e}(\theta_s)}{g_{\Sigma_e}(\theta_s)} \quad (62)$$

The quiescent sum and difference beampatterns in the elevation dimension can be given by

$$g_{\Sigma_e}(\theta_s) = (\mathbf{w}_{\Sigma_E})^H \mathbf{a}_{ze}(\theta_s) = \frac{1 - e^{j4\pi M \frac{d}{\lambda} (\sin \theta_s - \sin \theta_0)}}{1 - e^{j4\pi \frac{d}{\lambda} (\sin \theta_s - \sin \theta_0)}} \quad (63a)$$

$$\begin{aligned} g_{\Delta_e}(\theta_s) &= (\mathbf{w}_{\Delta_E})^H \mathbf{a}_{ze}(\theta_s) \\ &= \left( 1 - e^{j2\pi M \frac{d}{\lambda} (\sin \theta_s - \sin \theta_0)} \right) \frac{1 - e^{j2\pi M \frac{d}{\lambda} (\sin \theta_s - \sin \theta_0)}}{1 - e^{j4\pi \frac{d}{\lambda} (\sin \theta_s - \sin \theta_0)}} \end{aligned} \quad (63b)$$

Therefore, (62) can be further given by

$$\begin{aligned} \hat{m}_E &= \frac{g_{\Delta_e}(\theta_s)}{g_{\Sigma_e}(\theta_s)} = \frac{1 - e^{j2\pi M \frac{d}{\lambda} (\sin \theta_s - \sin \theta_0)}}{1 + e^{j2\pi M \frac{d}{\lambda} (\sin \theta_s - \sin \theta_0)}} \\ &\approx -j \tan \left[ \pi M \frac{d}{\lambda} \cos \theta_0 (\theta_s - \theta_0) \right] \end{aligned} \quad (64)$$

TABLE I: Parameters of Radar

Parameter	Value	Parameter	Value
Number of rows	16	Number of columns	16
Carrier frequency	10GHz	Element spacing	0.015m
Bandwidth	20MHz	Time shift	0.05 $\mu$ s
PRF	20KHz	Pulse width	10 $\mu$ s

TABLE II: Parameters of target and jammings

	Targe	MLJ1	MLJ2	SLJ
Azimuth angle( $^\circ$ )	0.5	3	-3	8
Elevation angle( $^\circ$ )	0.5	-3	3	-6
Range(km)	75.15	75.3	74.6	80.8
SNR/JNR(dB)	10	40	40	40

Similarly, the adaptive azimuth monopulse ratio and range monopulse ratio can be given by

$$\hat{m}_A \approx -j \tan \left[ \pi N \frac{d}{2\lambda} \cos \theta_0 \cos \varphi_0 (\varphi_s - \varphi_0) \right] \quad (65)$$

$$\hat{m}_R \approx -j \tan \left[ \pi \mu M \frac{\Delta t}{c} (R_s - R_0) \right] \quad (66)$$

Taking the imaginary part of these three adaptive monopulse ratios, the corresponding adaptive monopulse ratio curves can be obtained as

$$f(\theta_s) = \text{Im}(\hat{m}_E) = -\tan \left[ \pi M \frac{d}{\lambda} \cos \theta_0 (\theta_s - \theta_0) \right] \quad (67)$$

$$f(\varphi_s) = \text{Im}(\hat{m}_A) = -\tan \left[ \pi N \frac{d}{2\lambda} \cos \theta_0 \cos \varphi_0 (\varphi_s - \varphi_0) \right] \quad (68)$$

$$f(R_s) = \text{Im}(\hat{m}_R) = -\tan \left[ \pi \mu M \frac{\Delta t}{c} (R_s - R_0) \right] \quad (69)$$

where  $f(\theta_s)$ ,  $f(\varphi_s)$  and  $f(R_s)$  represent the adaptive monopulse ratio curves in the elevation, azimuth and range dimensions, respectively. These three adaptive monopulse ratio curves are univariate monotonic functions near the radar array pointing direction, each solely dependent on the corresponding target parameter. Thus, the target angle and range can be estimated by the corresponding adaptive monopulse ratio values.

## V. SIMULATION RESULTS

To fully validate the theoretical analysis of the two proposed algorithms, simulations are provided in this section. First, we evaluate the effectiveness of MLJ suppression for the two algorithms by examining the formation of nulls in the adaptive beampatterns. Second, the results of joint angle-range estimation and root mean square error (RMSE) are provided to assess the performance of monopulse parameters estimation.

Assume a planar array consisting of  $M \times N$  elements,  $M = N = 16$ , time shift is  $\Delta t = 1/B$  and the element spacing along the Y-axis and Z-axis is  $d = 0.5\lambda$ . The simulation parameters are listed in Table I.

### A. Performance in jamming suppression

The locations of target and jammings are given in Table II.

(1) Experiment with four-channel adaptive beamforming algorithm

In this experiment, we assume the presence of a target and MLJ1. Fig. 6 presents the adaptive elevation-sum beampattern. Fig. 6(a) shows a 3-D view of the adaptive elevation-sum beampattern, while Fig. 6(b) depicts its 2-D view. In Fig. 6(b), it is evident that a null zone is formed at an azimuth angle of  $3^\circ$ , precisely where the MLJ1 is located, indicating effective suppression of MLJ1 along the azimuth direction. Fig. 6(c) compares the beampatterns in azimuth dimension of the adaptive elevation-sum beam with that of the quiescent elevation-sum beam at an elevation angle of  $0^\circ$ . It can be seen that a null is formed in the beampattern in azimuth dimension of the adaptive elevation-sum beam at an azimuth angle of  $3^\circ$ , with a depth approaching  $-30\text{dB}$ , providing a more intuitive demonstration that the MLJ1 has been effectively suppressed along the azimuth direction. Fig. 6(d) compares the beampatterns in elevation dimension of the adaptive elevation-sum beam with that of the quiescent elevation-sum beam at an azimuth angle of  $0^\circ$ . It is evident that the beampattern in elevation dimension of the adaptive elevation-sum beam has been well maintained. To summarize, in the adaptive elevation-sum beam, the MLJ1 has been effectively suppressed along azimuth direction while keeping the beampattern undistorted along elevation direction.

Similarly, Fig. 7 presents the adaptive azimuth-sum beampattern. Fig. 7(a) shows a 3-D view of the adaptive azimuth-sum beampattern, while Fig. 7(b) depicts its 2-D view. In Fig. 7(b), it is evident that a null zone is formed at an elevation angle of  $-3^\circ$ , precisely where the MLJ1 is located, indicating effective suppression of MLJ1 along the elevation direction. Fig. 7(c) compares the beampatterns in azimuth dimension of the adaptive azimuth-sum beam with that of the quiescent azimuth-sum beam at an elevation angle of  $0^\circ$ . It is observed that the beampattern in azimuth dimension of the adaptive azimuth-sum beam has been well maintained. Fig. 7(d) compares the beampatterns in elevation dimension of the adaptive azimuth-sum beam with that of the quiescent azimuth-sum beam at an azimuth angle of  $0^\circ$ . It can be seen that a null is formed at an elevation angle of  $-3^\circ$ , with a depth approaching  $-41\text{dB}$ , providing a more intuitive demonstration that the MLJ1 has been effectively suppressed along the elevation direction. To summarize, in the adaptive azimuth-sum beam, the MLJ1 has been effectively canceled along elevation direction while keeping the beampattern undistorted along azimuth direction.

After setting  $\Delta t = 1/B$ , the planar array becomes an azimuth-range two-dimensional planar array. Fig. 8 presents the adaptive range-sum beampattern. Fig. 8(a) shows a 3-D view of the adaptive range-sum beampattern, while Fig. 8(b) shows its 2-D view. In Fig. 8(b), it is evident that a null zone is formed at an azimuth angle of  $3^\circ$ , precisely where the MLJ1 is located, indicating effective suppression of MLJ1 along the azimuth direction. Fig. 8(c) compares the beampatterns in azimuth dimension of the adaptive range-sum beam with that of the quiescent range-sum beam at a range of  $75\text{km}$ . It can be seen that a null is formed in the beampattern in azimuth dimension of the adaptive range-sum beam at



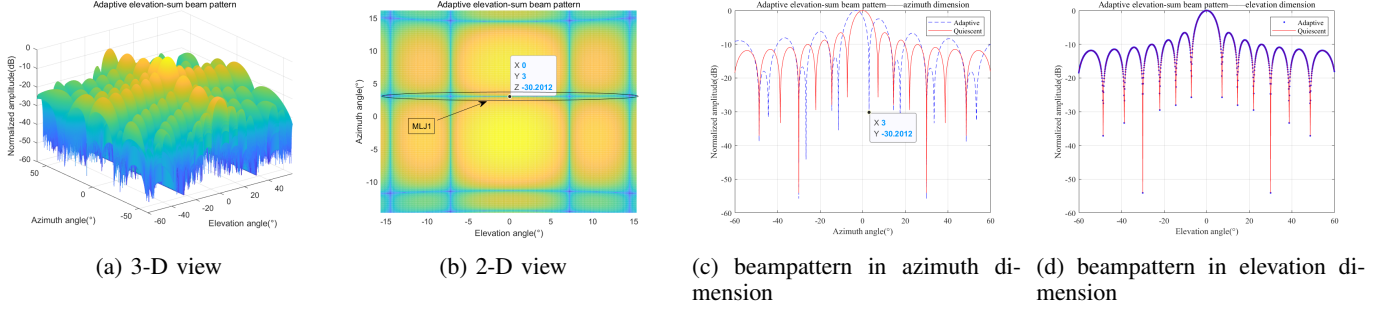


Fig. 6. Adaptive elevation-sum beam pattern

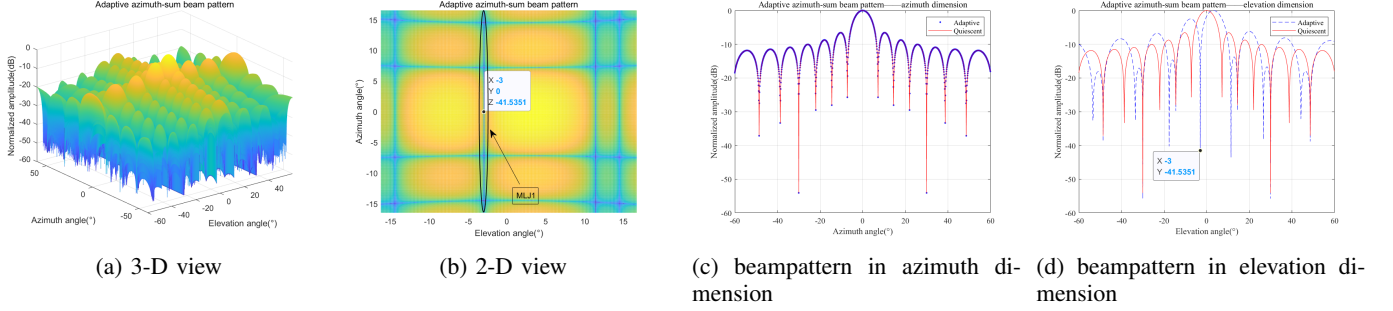


Fig. 7. Adaptive azimuth-sum beam pattern

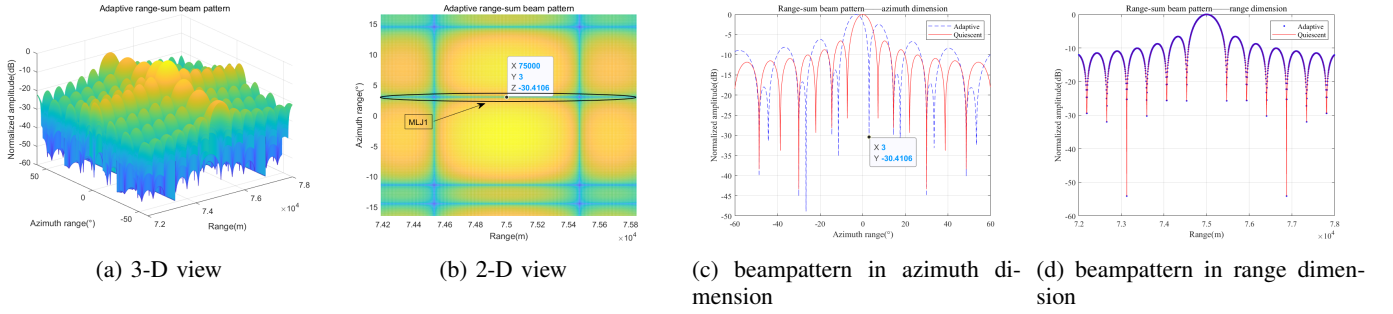


Fig. 8. Adaptive range-sum beam pattern

an azimuth angle of  $3^\circ$ , with a depth approaching  $-30\text{dB}$ , providing a more intuitive demonstration that the MLJ1 has been effectively suppressed along the azimuth direction. Fig. 8(d) compares the beam patterns in range dimension of the adaptive range-sum beam with that of the quiescent range-sum beam at an azimuth angle of  $0^\circ$ . As shown in this figure, the beam pattern in range dimension of the adaptive range-sum beam has been well maintained. In brief, the MLJ1 has been effectively canceled along azimuth direction while keeping the beam pattern undistorted along range direction.

#### (2) Experiment with row-column adaptive beamforming algorithm

In this experiment, we consider a target, two MLJs and a SLJ. The planar array is divided into  $4 \times 4$  subarrays, with 4 elements along both the Y-axis and the Z-axis in each subarray. First, analog beamforming at element level and converting each subarray output into digital signal. Second, ABF in each row and column with four subarray beam outputs. Therefore, four DOFs have been exploited to suppress jammings, making

it possible to suppress three jammings at most.

Fig. 9 presents the adaptive elevation-sum beam pattern. Fig. 9(a) shows a 3-D view of the adaptive elevation-sum beam pattern, while Fig. 9(b) shows its 2-D view. In Fig. 9(b), it is evident that three null zones are formed at azimuth angles of  $-3^\circ$ ,  $3^\circ$  and  $8^\circ$ , precisely where the two MLJs and a SLJ are located. This indicates effective suppression of multiple jammings along the azimuth direction. Fig. 9(c) compares the beam patterns in azimuth dimension of the adaptive elevation-sum beam with that of the quiescent elevation-sum beam at an elevation angle of  $0^\circ$ . It can be seen that three nulls are formed in the beam pattern in azimuth dimension of the adaptive elevation-sum beam at azimuth angles of  $-3^\circ$ ,  $3^\circ$  and  $8^\circ$ , providing a more intuitive demonstration that the multiple jammings have been effectively suppressed along the azimuth direction. Fig. 9(d) compares the beam patterns in elevation dimension of the adaptive elevation-sum beam with that of the quiescent elevation-sum beam at an azimuth angle of  $0^\circ$ . It is evident that the beam pattern in elevation

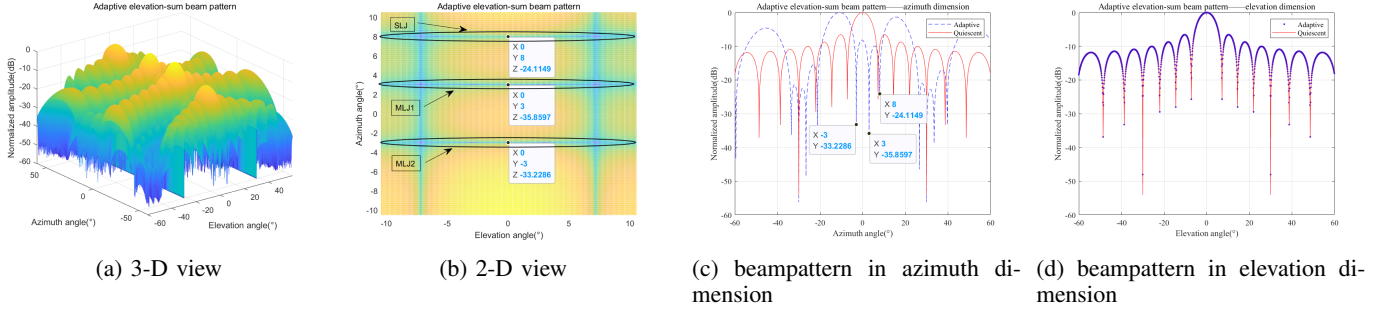


Fig. 9. Adaptive elevation-sum beam pattern

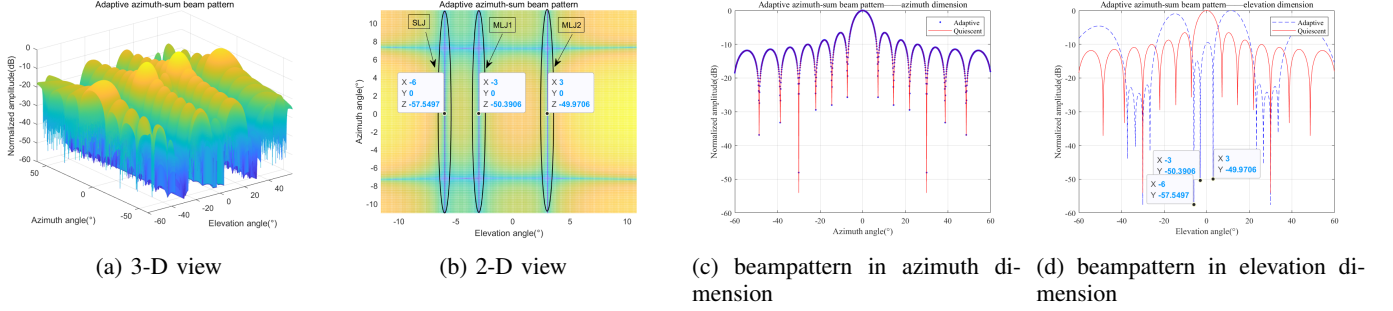


Fig. 10. Adaptive azimuth-sum beam pattern

dimension of the adaptive elevation-sum beam has been well maintained. To sum up, in the adaptive elevation-sum beam, the multiple jammings have been effectively canceled along azimuth direction while keeping the beam pattern undistorted along elevation direction.

Fig. 10 presents the adaptive azimuth-sum beam pattern. Fig. 10(a) shows a 3-D view of the adaptive azimuth-sum beam pattern, while Fig. 10(b) depicts its 2-D view. In Fig. 10(b), it is evident that three null zones are formed at elevation angles of  $-6^\circ$ ,  $-3^\circ$  and  $3^\circ$ , precisely where the two MLJs and a SLJ are located, indicating effective suppression of multiple jammings along the elevation direction. Fig. 10(c) compares the beam patterns in azimuth dimension of the adaptive azimuth-sum beam with that of the quiescent azimuth-sum beam at an elevation angle of  $0^\circ$ . As shown, the beam pattern in azimuth dimension of the adaptive azimuth-sum beam has been well maintained. Fig. 10(d) compares the beam patterns in elevation dimension of the adaptive azimuth-sum beam with that of the quiescent azimuth-sum beam at an azimuth angle of  $0^\circ$ . It can be seen that three nulls are formed in the beam pattern in elevation dimension of the adaptive azimuth-sum beam at elevation angles of  $-6^\circ$ ,  $-3^\circ$  and  $3^\circ$ . This further demonstrates that the multiple jammings have been effectively suppressed along the elevation direction. To summarize, in the adaptive azimuth-sum beam, the multiple jammings have been effectively canceled along elevation direction while keeping the beam pattern undistorted along azimuth direction.

After setting  $\Delta t = 1/B$ , the planar array becomes an azimuth-range two-dimensional planar array. Fig. 11 presents the adaptive range-sum beam pattern. Fig. 11(a) shows a 3-D view of the adaptive range-sum beam pattern, while Fig. 11(b) depicts its 2-D view. In Fig. 11(b), three null zones

are formed at azimuth angles of  $-3^\circ$ ,  $3^\circ$  and  $8^\circ$ , precisely where the two MLJs and a SLJ are located, indicating effective suppression of multiple jammings along the azimuth direction. Fig. 11(c) compares the beam patterns in azimuth dimension of the adaptive range-sum beam with that of the quiescent range-sum beam at a range of  $75\text{km}$ . It can be seen that three nulls are formed in the beam pattern in azimuth dimension of the adaptive range-sum beam at azimuth angles of  $-3^\circ$ ,  $3^\circ$  and  $8^\circ$ . This further clarifies that the multiple jammings have been effectively suppressed along the azimuth direction. Fig. 11(d) compares the beam patterns in range dimension of the adaptive range-sum beam with that of the quiescent range-sum beam at an azimuth angle of  $0^\circ$ . It is evident that the beam pattern in range dimension of the adaptive range-sum beam has been well maintained. In conclusion, the multiple jammings have been effectively suppressed along azimuth direction while keeping the beam pattern undistorted along range direction.

### B. Performance in parameters estimation

After suppressing jamming, the adaptive sum-and-difference beams are used for monopulse parameters estimation. The target angle or range is then retrieved by mapping the adaptive monopulse ratio to the corresponding curve.

Fig. 12 compares the quiescent monopulse ratio curves with the adaptive monopulse ratio curves obtained using the four-channel ABF algorithm in the elevation, azimuth and range dimensions, respectively, along with the corresponding parameter estimation results. In Fig. 12(a), the quiescent and adaptive monopulse ratio curves in elevation dimension are completely consistent, indicating that MLJ suppression does not cause distortion in monopulse ratio. Additionally, the elevation angle estimation result is  $0.50178^\circ$ , with an error

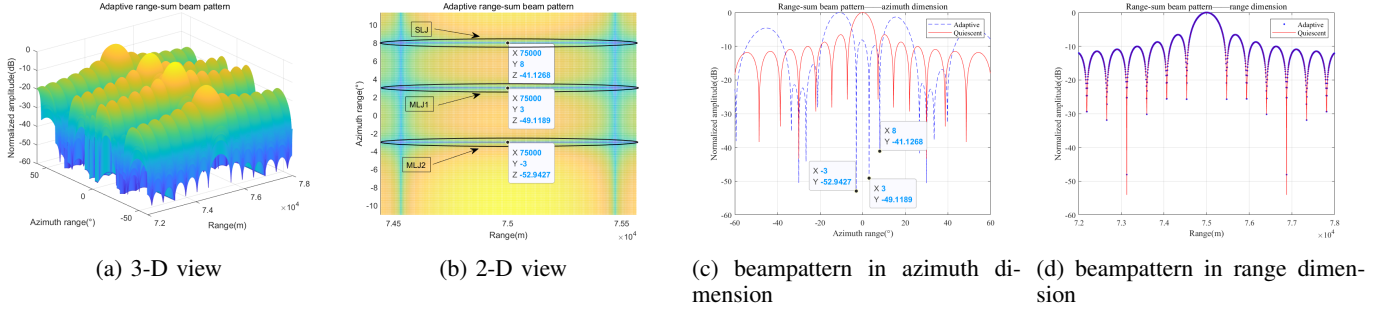


Fig. 11. Adaptive range-sum beampattern

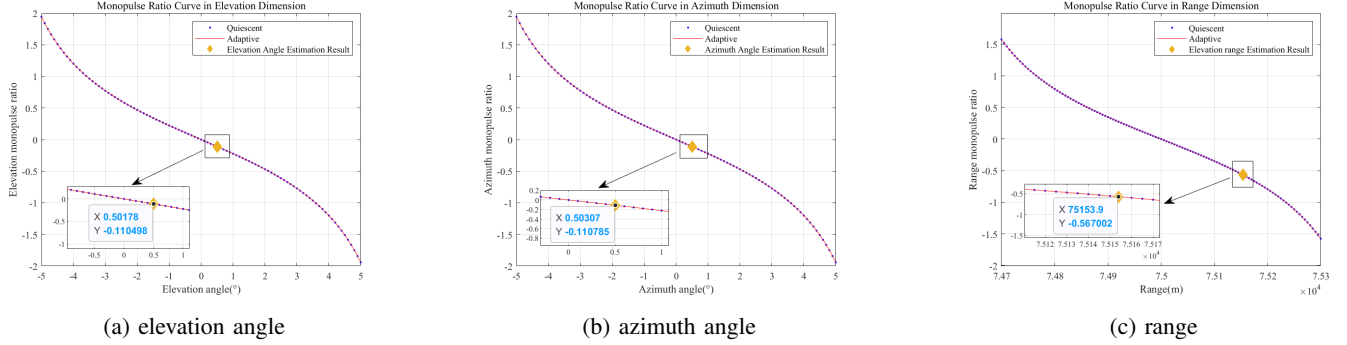


Fig. 12. Monopulse ratio curve and parameters estimation result using four-channel ABF algorithm

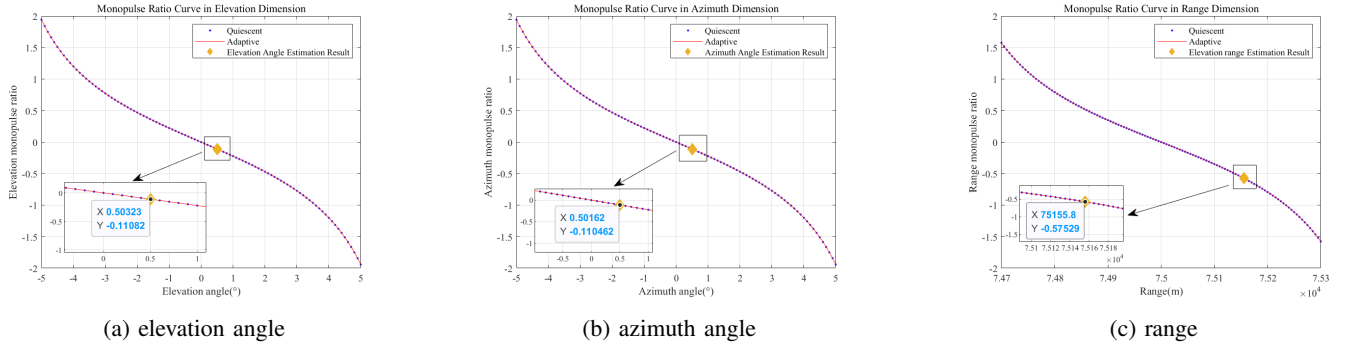


Fig. 13. Monopulse ratio curve and parameters estimation result using row-column ABF algorithm

of  $0.00178^\circ$  compared to the true target elevation angle. Similarly, in Fig. 12(b) and Fig. 12(c), the adaptive azimuth angle monopulse ratio curve is maintained, as is the adaptive range monopulse ratio curve. The azimuth angle estimation result is  $0.50307^\circ$ , the range estimation result is  $75.1539km$ , both very close to the parameters of the target location.

Similar to Fig. 12, Fig. 13 compares the quiescent monopulse ratio curves with the adaptive monopulse ratio curves obtained using the row-column ABF algorithm. It can be seen that the quiescent and adaptive monopulse ratio curves in all three dimensions are completely consistent, indicating that multiple jammings suppression does not cause distortion in monopulse ratio. Further, the estimation result for the elevation angle, azimuth angle and range are  $0.50323^\circ$ ,  $0.50162^\circ$  and  $75.1558km$ , respectively, with errors of  $0.00323^\circ$ ,  $0.00162^\circ$  and  $5.8m$  compared to the true parameters of the target.

Moreover, the RMSEs of angle estimation and range esti-

mation are shown in Fig. 14, which can be defined as

$$RMSE_\theta = \sqrt{\frac{1}{L} \sum_{l=1}^L (\hat{\theta}_l - \theta_s)^2} \quad (70a)$$

$$RMSE_\varphi = \sqrt{\frac{1}{L} \sum_{l=1}^L (\hat{\varphi}_l - \varphi_s)^2} \quad (70b)$$

$$RMSE_R = \sqrt{\frac{1}{L} \sum_{l=1}^L (\hat{R}_l - R_s)^2} \quad (70c)$$

where  $\hat{\theta}_l$ ,  $\hat{\varphi}_l$  and  $\hat{R}_l$  denote the estimated elevation angle, azimuth angle and range in the  $l$ th Monte-Carlo experiment, and  $L$  denotes the total number of Monte-Carlo experiments. This study conducts 1000 Monte-Carlo experiments.

As shown in Fig. 14(a) and Fig. 14(b), it can be clearly seen that the RMSE of angle estimation decreases as the

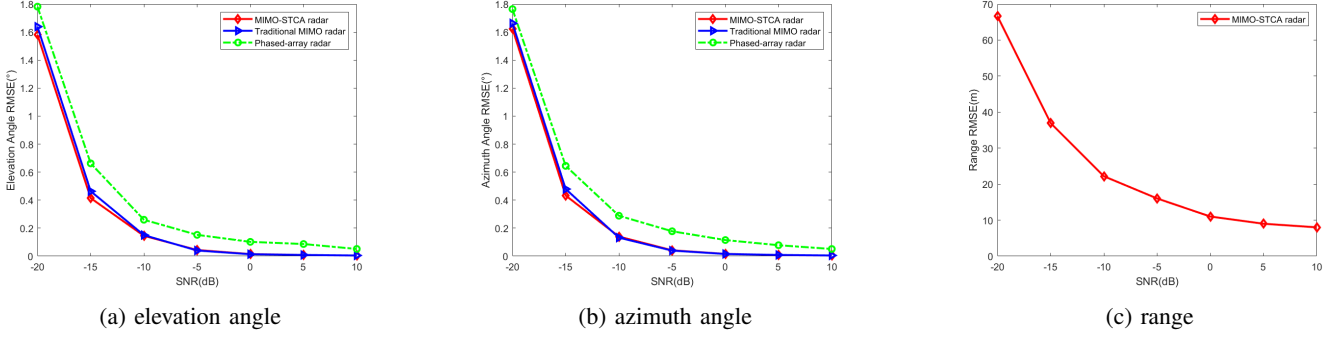


Fig. 14. RMSEs of parameter estimation versus SNR

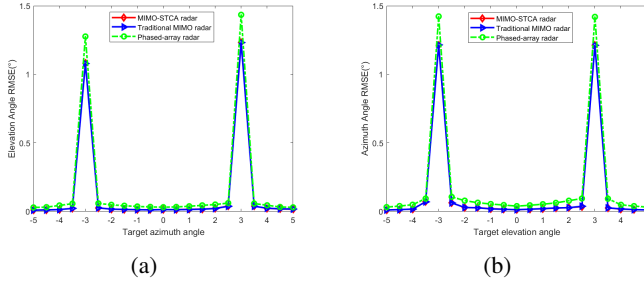


Fig. 15. RMSEs of parameter estimation vary with the target position (a) elevation angle (b) azimuth angle

SNR increases. The RMSEs of the traditional MIMO radar and the MIMO-STCA radar are similar and both outperform that of the Phased-array radar. Since the traditional MIMO radar and the Phased-array radar cannot extract range information, monopulse technique cannot be applied for range parameter estimation. Therefore, only the RMSE of range estimation with MIMO-STCA radar is shown in Fig. 14(c). It is evident that the RMSE of range estimation also decreases with the increase in SNR, and stays at a relatively low error level.

Fig. 15 shows the results of the angle estimation RMSE as the target angle changes, in the presence of MLJ1 and MLJ2. It can be observed that the angle estimation error increases as the target approaches the MLJ. Notably, the performance of the traditional MIMO radar and the MIMO-STCA radar are similar, both outperforming the Phased-array radar.

## VI. CONCLUSIONS

In this paper, we addressed the challenges of mainlobe jamming suppression and joint angle-range estimation in monopulse radar systems by proposing a novel MIMO-STCA framework integrated with adaptive beamforming techniques. To achieve accurate parameter estimation under complex jamming scenarios, we developed two key algorithms: a four-channel ABF method that introduces an additional delta-delta channel for single MLJ suppression while preserving monopulse ratio integrity, and a hierarchical row-column ABF algorithm that leverages subarray-level spatial DOFs to simultaneously mitigate multiple MLJs and SLJs. The proposed MIMO-STCA architecture exploits time-shifted transmissions across array rows to create range-domain DOFs, enabling

joint angle-range estimation through monopulse processing. Theoretical analysis confirmed that both algorithms maintain undistorted sum and difference beampatterns along orthogonal spatial directions during interference suppression, while numerical simulations demonstrated precise null steering toward jammer locations and consistent monopulse ratio preservation. Experimental validation showed significant improvements in estimation accuracy, with RMSEs reduced by over 10%-60% compared to the Phased-array radar in MLJ scenarios. Future research directions may focus on real-time implementation of the proposed algorithms for dynamic jamming environments and extension of the framework to multi-target scenarios.

## REFERENCES

- [1] S. M. Sherman and D. K. Barton, *Monopulse principles and techniques*. Artech House, 2011.
- [2] U. Nickel, "Overview of generalized monopulse estimation," *IEEE Aerospace and Electronic Systems Magazine*, vol. 21, no. 6, pp. 27–56, 2006.
- [3] W.-C. Su, X.-X. Wu, T.-S. Horng, and M.-C. Tang, "Hybrid continuous-wave and self-injection-locking monopulse radar for posture and fall detection," *IEEE Transactions on Microwave Theory and Techniques*, vol. 70, no. 3, pp. 1686–1695, 2022.
- [4] H. Wu, R. Liu, Y. Guo, J. Zhang, F. He, and J. Meng, "Performance analysis of mainlobe canceller for monopulse at subarray level in the presence of amplitude-phase error," *IEEE Transactions on Aerospace and Electronic Systems*, 2024.
- [5] Z. Wang, A. Sinha, P. Willett, and Y. Bar-Shalom, "Angle estimation for two unresolved targets with monopulse radar," *IEEE Transactions on Aerospace and Electronic Systems*, vol. 40, no. 3, pp. 998–1019, 2004.
- [6] Y. Liu, L. Zhou, F. He, D. Li, and J. Meng, "Probabilistic analysis of the amplitude-phase error tolerance for cross-eye jamming," *IEEE Transactions on Aerospace and Electronic Systems*, vol. 59, no. 1, pp. 678–684, 2022.
- [7] X. Hong, Z. Liang, Y. Song, and S. Hu, "Angular glint analysis based on parametric model of target," in *2019 IEEE International Conference on Signal, Information and Data Processing (ICSIDP)*. IEEE, 2019, pp. 1–6.
- [8] A. Al-Khawaja and S. B. Sadkhan, "Intelligence and electronic warfare: challenges and future trends," in *2021 7th International Conference on Contemporary Information Technology and Mathematics (ICCITM)*. IEEE, 2021, pp. 118–123.
- [9] X. Chen, T. Shu, K.-B. Yu, and W. Yu, "Enhanced adbf architecture for monopulse angle estimation in multiple jamming," *IEEE Antennas and Wireless Propagation Letters*, vol. 16, pp. 2684–2687, 2017.
- [10] I. Mallioras, Z. D. Zaharis, P. I. Lazaridis, and S. Pantelopoulou, "A novel realistic approach of adaptive beamforming based on deep neural networks," *IEEE Transactions on Antennas and Propagation*, vol. 70, no. 10, pp. 8833–8848, 2022.



- [11] S. Dai, M. Li, Q. H. Abbasi, and M. A. Imran, "A fast blocking matrix generating algorithm for generalized sidelobe canceller beamformer in high speed rail like scenario," *IEEE Sensors Journal*, vol. 21, no. 14, pp. 15 775–15 783, 2020.
- [12] Q. He, Z. Cheng, Z. Wang, and Z. He, "Performance analysis and improvement of constrained adaptive monopulse approach," *IEEE Signal Processing Letters*, 2023.
- [13] B. Han, X. Yang, T. Lan, and W. Pu, "Mainlobe jamming suppression method based on beamspace orthogonal cancellation for distributed array radar," *IET Conference Proceedings*, vol. 2020, pp. 844–847, 2021.
- [14] Y. Lu, J. Ma, J. Zhou, and L. Shi, "Adaptive polarization-constrained monopulse approach for dual-polarization array," *IEEE Antennas and Wireless Propagation Letters*, vol. 20, no. 3, pp. 289–292, 2020.
- [15] K.-B. Yu and D. J. Murrow, "Adaptive digital beamforming for preserving monopulse target angle estimation accuracy in jamming," in *Proceedings of the 2000 IEEE Sensor Array and Multichannel Signal Processing Workshop. SAM 2000 (Cat. No. 00EX410)*. IEEE, 2000, pp. 454–458.
- [16] H. Dai, X. Wang, Y. Li, Y. Liu, and S. Xiao, "Main-lobe jamming suppression method of using spatial polarization characteristics of antennas," *IEEE Transactions on Aerospace and Electronic Systems*, vol. 48, no. 3, pp. 2167–2179, 2012.
- [17] M. Ge, G. Cui, X. Yu, and L. Kong, "Main lobe jamming suppression via blind source separation sparse signal recovery with subarray configuration," *IET radar, sonar & navigation*, vol. 14, no. 3, pp. 431–438, 2020.
- [18] B. Zhou, R. Li, W. Liu, Y. Wang, L. Dai, and Y. Shao, "A bss-based space-time multi-channel algorithm for complex-jamming suppression," *Digital Signal Processing*, vol. 87, pp. 86–103, 2019.
- [19] X. Yang, P. Yin, T. Zeng, and T. K. Sarkar, "Applying auxiliary array to suppress mainlobe interference for ground-based radar," *IEEE Antennas and Wireless Propagation Letters*, vol. 12, pp. 433–436, 2013.
- [20] L. Zhang, L. Su, D. Wang, Y. Luo, and Q. Zhang, "Mainlobe interference suppression for radar network via rpca-based covariance matrix reconstruction," *IEEE Sensors Journal*, vol. 23, no. 5, pp. 5094–5108, 2023.
- [21] Z. Cheng, Z. He, X. Duan, X. Zhang, and B. Liao, "Adaptive monopulse approach with joint linear constraints for planar array at subarray level," *IEEE Transactions on Aerospace and Electronic Systems*, vol. 54, no. 3, pp. 1432–1441, 2018.
- [22] J. Li and P. Stoica, *MIMO radar signal processing*. John Wiley & Sons, 2008.
- [23] J. Yang, B. Wang, Z. Chang, Y. Zhao, Z. Feng, and F. Hu, "Joint trajectory planning and transmit resource optimization for multi-target tracking in multi-uav-enabled mimo radar system," *IEEE Transactions on Intelligent Transportation Systems*, 2024.
- [24] Y. Li, Y. Zhou, X. Li, J. Wang, Y. Wang, L. Fan, and F.-Y. Wang, "Unimodular complete complementary sequence with optimal trade-off between auto-and cross-ambiguity functions for mimo radars," *IEEE Transactions on Intelligent Vehicles*, 2024.
- [25] J. Li and P. Stoica, "Mimo radar with colocated antennas," *IEEE signal processing magazine*, vol. 24, no. 5, pp. 106–114, 2007.
- [26] A. Ajourloo, A. Amini, E. Tohidi, M. H. Bastani, and G. Leus, "Antenna placement in a compressive sensing-based colocated mimo radar," *IEEE Transactions on Aerospace and Electronic Systems*, vol. 56, no. 6, pp. 4606–4614, 2020.
- [27] E. Tohidi, M. Coutino, S. P. Chepuri, H. Behroozi, M. M. Nayebi, and G. Leus, "Sparse antenna and pulse placement for colocated mimo radar," *IEEE Transactions on Signal Processing*, vol. 67, no. 3, pp. 579–593, 2018.
- [28] H. Wang, Y. Quan, G. Liao, S. Zhu, J. Xu, and L. Huang, "Space-time coding technique for coherent frequency diverse array," *IEEE Transactions on Signal Processing*, vol. 69, pp. 5994–6008, 2021.
- [29] Y. Liu, P. Wang, Z. Men, Y. Guo, T. He, R. Bao, and L. Cui, "A signal model based on the space-time coding array and a novel imaging method based on the hybrid correlation algorithm for f-scan sar," *Remote Sensing*, vol. 15, no. 17, p. 4276, 2023.
- [30] L. Zhang, X. Q. Chen, S. Liu, Q. Zhang, J. Zhao, J. Y. Dai, G. D. Bai, X. Wan, Q. Cheng, G. Castaldi *et al.*, "Space-time-coding digital metasurfaces," *Nature communications*, vol. 9, no. 1, p. 4334, 2018.
- [31] H. Wang, G. Liao, Y. Zhang, J. Xu, S. Zhu, and L. Huang, "Transmit beampattern synthesis for chirp space-time coding array by time delay design," *Digital Signal Processing*, vol. 110, p. 102901, 2021.
- [32] G. Babur, P. Aubry, and F. Le Chevalier, "Space-time radar waveforms: circulating codes," *Journal of Electrical and Computer Engineering*, vol. 2013, no. 1, p. 809691, 2013.
- [33] H. Wang, G. Liao, J. Xu, S. Zhu, and C. Zeng, "Direction-of-arrival estimation for circulating space-time coding arrays: From beamspace music to spatial smoothing in the transform domain," *Sensors*, vol. 18, no. 11, p. 3689, 2018.
- [34] S. Li, N. Liu, L. Zhang, J. Zhang, S. Tang, and X. Huang, "Transmit beampattern synthesis for mimo radar using extended circulating code," *IET Radar, Sonar & Navigation*, vol. 12, no. 6, pp. 610–616, 2018.
- [35] F. C. Robey, S. Coutts, D. Weikle, J. C. McHarg, and K. Cuomo, "Mimo radar theory and experimental results," in *Conference Record of the Thirty-Eighth Asilomar Conference on Signals, Systems and Computers, 2004.*, vol. 1. IEEE, 2004, pp. 300–304.
- [36] G. San Antonio, D. R. Fuhrmann, and F. C. Robey, "Mimo radar ambiguity functions," *IEEE Journal of Selected Topics in Signal Processing*, vol. 1, no. 1, pp. 167–177, 2007.
- [37] L. Xu, J. Li, and P. Stoica, "Adaptive techniques for mimo radar," in *Fourth IEEE Workshop on Sensor Array and Multichannel Processing, 2006*. IEEE, 2006, pp. 258–262.
- [38] L. Xu, S. Zhou, H. Liu, and J. Liu, "Repeat radar jammer suppression for a colocated mimo radar," *IET Radar, Sonar & Navigation*, vol. 13, no. 9, pp. 1448–1457, 2019.
- [39] E. Raci, M. Alaei-Kerahroodi, P. Babu, and M. B. Shankar, "Generalized waveform design for sidelobe reduction in mimo radar systems," *Signal Processing*, vol. 206, p. 108914, 2023.
- [40] X. Wang, W. Zhai, X. Zhang, X. Wang, and M. G. Amin, "Enhanced automotive sensing assisted by joint communication and cognitive sparse mimo radar," *IEEE Transactions on Aerospace and Electronic Systems*, vol. 59, no. 5, pp. 4782–4799, 2023.
- [41] Z. Xu and A. Petropulu, "A bandwidth efficient dual-function radar communication system based on a mimo radar using ofdm waveforms," *IEEE Transactions on Signal Processing*, vol. 71, pp. 401–416, 2023.

**Huake Wang** received the B.S. degree in electronics engineering, and the Ph.D. degree in signal and information processing from Xidian University, Xi'an, China, in 2015 and 2020, respectively. She was a Visiting Ph.D. Student with the Department of Electrical Engineering, Columbia University, New York, from 2020 to 2021. Currently, she is an Associate Professor with the School of Electronics Engineering, Xidian University. Her research interests include signal processing, new concept radar and intelligent sensing.

**Dongchang Zhang** received the B.S. degree in Electronic Information Engineering from China Jil-jiang University in 2023. He is currently pursuing a master's degree in Information and Communication Engineering at Hangzhou Research Institute of Xidian University. His research interests include radar signal processing, jamming suppression and electronic countermeasures.

**Guisheng Liao** (Senior Member, IEEE) was born in Guilin, Guangxi, China in 1963. He received the B.S. degree from Guangxi University in mathematics, Guangxi, China, in 1985, and the M.S. degree in computer software and the Ph.D. degree in signal and information processing from Xidian University, Xi'an, China, in 1990, and 1992, respectively.

He has been a Senior Visiting Scholar with the Chinese University of Hong Kong from 1999 to 2000. He won the National Science Fund for Distinguished Young Scholars in 2008. His research interests include array signal processing, space-time adaptive processing, radar waveform design, and airborne/space surveillance and warning radar systems.

**Yinghui Quan** (Senior Member, IEEE) received the B.S. and Ph.D. degrees in electrical engineering from Xidian University, Xi'an, China, in 2004 and 2012, respectively.

He is currently a Full Professor with the Department of Remote Sensing Science and Technology, School of Electronic Engineering, Xidian University. His research interests include intelligent sensing and agile radar.

